Materials Characterization 202 (2023) 113024

Contents lists available at ScienceDirect

Materials Characterization

journal homepage: www.elsevier.com/locate/matchar

Laser surface treatment of Inconel 617 for next-generation nuclear reactors: A strengthening mechanisms study

Noah Holtham, Keivan Davami *

Department of Mechanical Engineering, The University of Alabama, Tuscaloosa, AL, USA

ARTICLE INFO

Keywords:
Laser peening
Inconel alloy 617
Taylor hardening
Precipitation strengthening

ABSTRACT

With the recent acceptance of Inconel Alloy 617 (IN617) for use under the ASME boiler and pressure vessel nuclear code, there is significant interest in developing manufacturing methods that can further magnify its effectiveness in intense thermo-mechanical loading scenarios. In this work, one such method, known as laser peening, was utilized in tandem with thermal aging to determine the relationship between the dislocation-rich microstructure following laser peening and the precipitation behavior of the strengthening phases. Results show that surface hardness after laser peening alone increased to 226 HV over the as-cast value of 195 HV. Following an aging heat treatment, the microhardness of the entire specimen and the laser peened zone increased by an additional 20%. Microstructural investigations revealed no change in grain size or orientation, though the precipitation of carbides throughout the microstructure resulted in a more homogenous dispersion after aging. Transmission electron microscopy revealed a rich dispersion of nanoscale γ' phases with an average area fraction of 12.5%, in addition to a high density of dislocations (3×10^{14} lines/m^2) near the laser peened surface. The Jackson-Reed model of precipitate strengthening was used in tandem with the Taylor hardening relationship to determine the effects of γ' strengthening and work hardening respectively. Both models were able to closely approximate the experimentally observed hardness data, leading to the conclusion that major surface strengthening effects result from (i) the precipitation of γ', and (ii) work hardening effects, with minor strengthening effects coming from (iii) residual stresses, and (iv) carbide strengthening. The results outlined herein present a promising, proof-of-concept for the use of laser peening to introduce surface mechanical property enhancement for IN617, a prime candidate material for next-generation nuclear reactor applications.

1. Introduction

Very high-temperature reactors (VHTRs) are next-generation (4th generation) graphite-moderated, helium-cooled nuclear power systems aimed for use in electricity and hydrogen production and are hailed for their safety, economical design, efficiency, and high-power output in comparison to 3rd generation reactors [1]. As the name suggests, VHTRs receive the majority of their efficiency improvement through the introduction of significantly increased turbine outlet temperatures of approximately 1000 °C. This leads to greatly improved thermal efficiencies compared to 3rd generation pressurized light water reactors which have typical outlet temperatures of around 400 °C. In addition to power generation, the high coolant temperatures of VHTRs can supply process heat for hydrogen production which is far more efficient than traditional fossil fuel combustion-based methods. Although VHTRs are very promising for the future of nuclear power technology, the tortuously high temperatures inherent to their design necessitate the usage of novel, high-performance materials which remain mechanically robust at elevated thermal loads while resisting wear and corrosion damage. To address this issue, section III of the ASME Boiler and Pressure Vessel code was recently updated to include a new alloy, IN617 or Alloy 617, as a validated material for nuclear reactor components [2] and is now under vigorous investigation for its use in VHTRs [3,4].

IN617 is an austenitic Ni-22Cr-12Co-9Mo solid solution alloy that exhibits exceptional oxidation resistance, mechanical properties, and high-temperature phase stability [5]. From a microstructural perspective, the superior high-temperature behavior of IN617 (> 800 °C) is attributed to the solution strengthening by molybdenum and cobalt, as well as the nucleation of strengthening $M_{23}C_6$ carbides [5]. Additionally, the inclusion of low weight-percentages of aluminum (<1%) provides further enhancement by strengthening the nickel matrix (γ) through the formation of intermetallic Ni_3Al type γ' [5] (though this is only a minor

* Corresponding author.
E-mail address: kdavami@eng.ua.edu (K. Davami).

https://doi.org/10.1016/j.matchar.2023.113024
Received 22 February 2023; Received in revised form 12 May 2023; Accepted 17 May 2023
Available online 18 May 2023

strengthening mechanism with the major role of aluminum solutes being the mitigation of high-temperature oxidation and carburization) [6]. In comparison to other prominent Ni-based superalloys such as Inconel 625 or 718, Inconel 617 differs in that it does not form detrimental topologically close-packed (TCP) phases when subjected to lengthy thermal exposures which typically result in crack nucleation following sufficient dislocation pileup at the particle interface [3]. Given its high-temperature stability, IN617 seems a choice material for VHTR valve and control rod applications. In several recent studies, the tribological performance of IN617 was tested [7–10] and it was found that IN617 generally performed favorably with higher contact friction and lower wear. However, issues with high contact friction, self-welding, and unique oxide formation were recorded, and therefore, a surface-hardening technique could fortify the material's wear resistance [11]. Specifically, in [11], laser peening was found to provide enhancements to tribological characteristics and was recommended as a topic for further research.

Laser peening (LP) is a post-processing mechanical surface modification technique aimed at improving a material's resistance to surface-related modes of failure including creep [12], fatigue [13], foreign impact damage [14,15], stress corrosion cracking [16,17], and wear [18,19] through the introduction of high magnitude compressive residual stresses and surface hardening. In contrast to other surface hardening methods, LP has a unique advantage in its ability to accommodate complex part geometries, with the only requirement being that the laser maintains line-of-sight to the part. While the process has been proven effective in a vast number of alloys, difficulties tend to arise at elevated temperatures. Relaxation of LP-induced residual stresses can occur around $0.5T_m$ (where T_m is the melting point of the material) due to the reorganization of dislocations within the work-hardened surface layer. Consequently, the elastically strained material underneath the surface begins to unload, causing a reduction in beneficial residual stresses. This limits the applicability of traditional LP to only low or ambient-temperature applications.

Despite instability at high temperatures, the advantages of LP are numerous. It follows that if the thermal degradation mechanisms can be mitigated, LP will be a prime candidate for applications where resistance to wear, fatigue, and foreign object damage are critical. Thus, significant interest has been placed on combining LP with a heat treatment step (either intermediate or concurrent with LP) [20–24]. The theory behind these works is that the integration of an aging step drives diffusion kinetics to enhance dislocation pinning effects within the plastically deformed zone via heterogeneous nucleation [20,21], and/or dynamic strain aging [22–24]. Notably, Munther et al. demonstrated that a cyclic aging / LP treatment (coined laser peening plus thermal microstructure engineering, LP + TME) on additively manufactured Inconel 718 retained 58% more of its residual stresses than traditional LP following a 350-h exposure to 600 °C ($0.5*T_m$ of Inconel 718) [20]. Additionally, the surface hardness of the LP + TME treated sample decreased only by 3% after high-temperature exposure. Electron microscopy investigations revealed the precipitation of strengthening phases within the dislocation-rich areas of the LP-affected region which helped reduce dislocation mobility and harden the material. Preliminary data from LP + TME experiments show the potential for LP in high-temperature applications through the addition of precipitation hardening mechanisms within the work-hardened layer.

Given its success in similar Ni-based superalloys, it is hypothesized by the authors of this work that conducting LP in tandem with a heat treatment stage on IN617 will lead to favorable alterations in surface mechanical strength. Thus, it is the goal of this work to develop a post-processing method that enhances the surface strength of IN617 and allows VHTR components crafted from this material to survive their harsh operating environments for longer and maximize their service life potential.

2. Experimental methods

2.1. Laser peening and heat treatment

IN617 samples were sectioned from the bulk material into 25 mm × 25 mm × 25 mm cubes using electron discharge machining (EDM) prior to treatment. The specimens examined in this work underwent either no treatment (as-cast), LP (LP), heat treatment (as-cast + HT), or a combination of both LP and heat treatment (LP + HT) (Table 1). LP (Fig. 1a and b) was carried out using a 1064 nm flash-pumped Nd glass laser delivering 3 J per pulse on target, with a beam irradiance of 2 GW/cm^2 at the University of Alabama, Tuscaloosa, USA. A circular 4.75 mm diameter spot and 8 ns pulse duration was utilized for all LP treatments. Aging treatments were performed with a 15 °C/min heating ramp rate and held for a duration of 60 h at 650 °C before furnace cooling at a rate of 1 °C/s (Fig. 1c and d). Additionally, a sample of unpeened material was placed in the furnace along with the LP samples to control for any change in mechanical properties caused solely by the heat treatment, rather than the combination of LP and heat treatment. Following each treatment routine, the samples were characterized via microhardness to determine the extent of surface property modifications caused by LP.

2.2. Specimen surface preparation

Following the various treatment schemes, samples were mounted in a conductive resin and were carefully ground with SiC paper (600–1200 grit) to remove macro-level imperfections and create a flat surface for mechanical testing and microscopy. Next, the samples were polished with diamond suspensions (9 μm – 1 μm) to remove scratches and plastically strained material created during the grinding phase. All surface polishing steps were conducted as lightly as possible to ensure the removal of minimal material from the treated surfaces. For specimens which were used for EBSD analysis, an additional vibratory polishing phase in a 0.25 μm diamond suspension was added to further enhance surface quality for accurate crystallographic readings. For specimens undergoing microscopic investigation, a solution of aqua regia was applied to the surface for 30 s (or until the microstructure was clearly visible).

2.3. Microhardness characterization

Microhardness tests were carried out to investigate the effectiveness of LP in delivering surface property improvement and to quantify the fidelity of observed hardness intensification following thermal exposure. Measurements were conducted using a Vickers microhardness tester (*Clemex Technologies Inc., Canada*) under a 300 gf (~3 N) applied load. A 30 × 5 indent pattern with 100 μm spacing was constructed to generate a microhardness distribution plot along the surface perpendicular to the irradiated regions.

2.4. Electron microscopy

Scanning electron microscopy (SEM, *Thermo Scientific Apreo FE-SEM*) was employed to visualize grain morphology following LP treatments as well as the presence of nucleated secondary phases. Electron backscatter detection (EBSD) was carried out to quantify grain size before and after LP and heat treatment, grain misorientation, and defect structures. A

Table 1
Sample identification details.

Sample ID	Laser peened	Aged
As-cast	–	–
LP	x	–
As-cast + HT	–	x
LP + HT	x	x

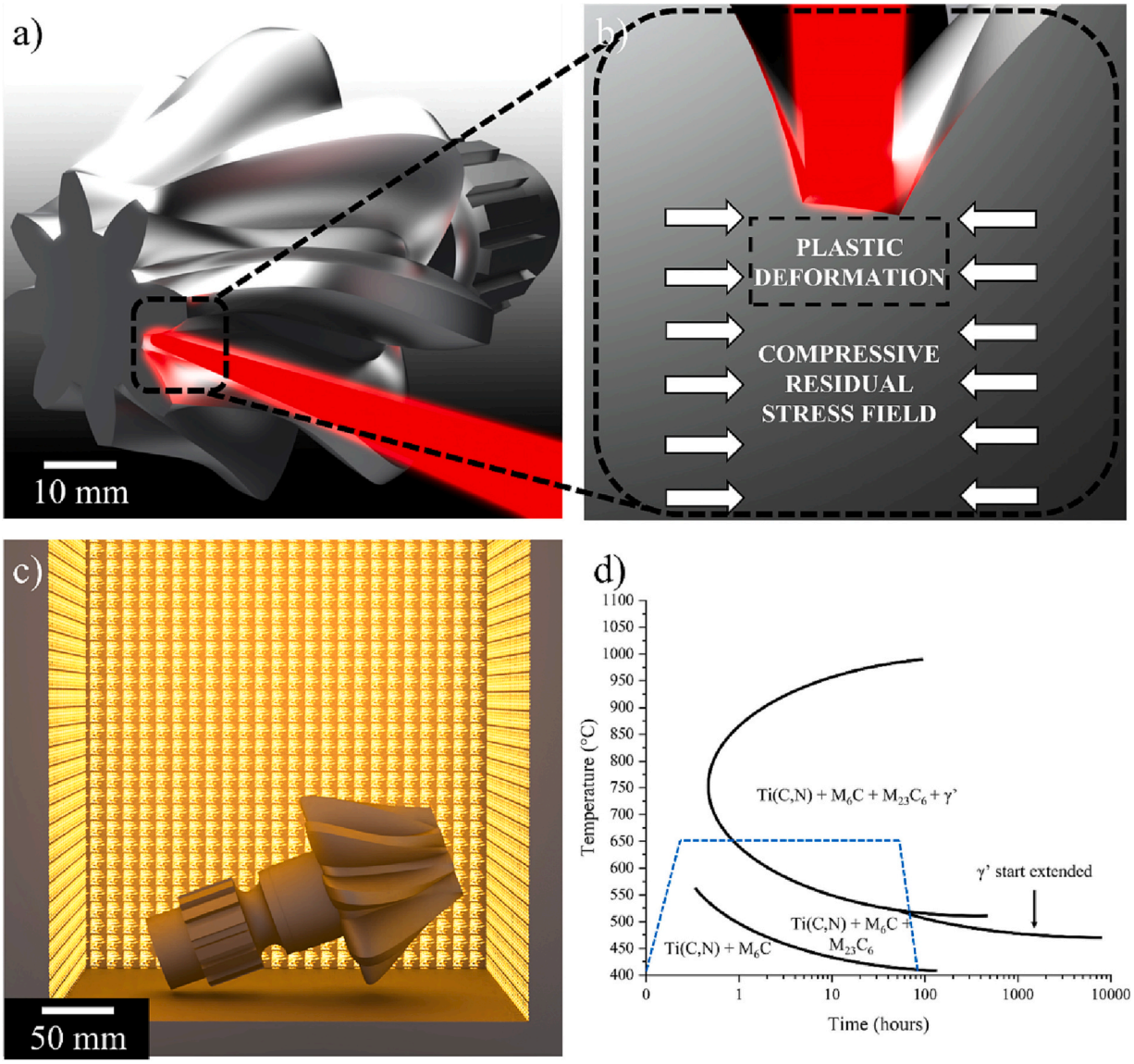

Fig. 1. (a) Illustration of the laser peening process with (b) a diagram depicting the plastically deformed zone and compressive residual stress field. (c) Illustration of the furnace heat treatment procedure and corresponding (d) Time-Temperature-Transformation (TTT) diagram for IN617 [25] with a blue dotted line showing the aging treatment conducted after LP in this work. (For interpretation of the references to colour in this figure legend, the reader is referred to the web version of this article.)

transmission electron microscope (TEM, FEI Tecnai F-20) with scanning transmission electron microscopy (STEM) capabilities were employed to study the interactions of dislocations and γ' precipitates. A focused ion beam (FIB, TESCAN LYRA FIB-FESEM) was used to precisely obtain thin foils from the LP surface as well as from the as-cast + HT specimen so that dislocations within the LPed microstructure and precipitate size and distribution could be determined.

2.5. X-ray diffraction

A Bruker D8 Discover X-Ray Diffractometer (XRD, *Bruker Corporation., USA*) with a $Co_{K\alpha 1}$ source and a 0.8 mm diameter aperture was used for phase identification.

3. Results

3.1. Microhardness

Fig. 2 shows the microhardness profile as a function of depth from the LPed surface as well as the hardness of the as-cast specimen. The untreated material (red dotted line) presented an average microhardness of 195 HV which increased by ~16% near the treated surface following LP. This increase can likely be attributed to the presence of work-hardening effects and compressive residual stresses, both of which provide resistance to localized plastic deformation. Following aging, the microhardness values showed a dramatic increase (solid blue line) within the LP-affected region from 226 HV to 292 HV at the surface as well as 195 HV to 235 HV throughout the bulk material (dotted blue line). Interestingly, the trend of hardness attenuation with increasing depths from the LP surface does not change following aging but is rather raised by a uniform value. The strengthening mechanisms contributing to this increase will be explored and discussed in following sections, however, it can be supposed from Fig. 2 that: (i) A combination of compressive residual stresses and work hardening are contributing to the increased resistance to plastic deformation at the LPed surface and that, (ii) An additional mechanism independent of LP was activated during the 650 °C / 60 h aging stage which further elevated the microhardness values of both the untreated and LPed material.

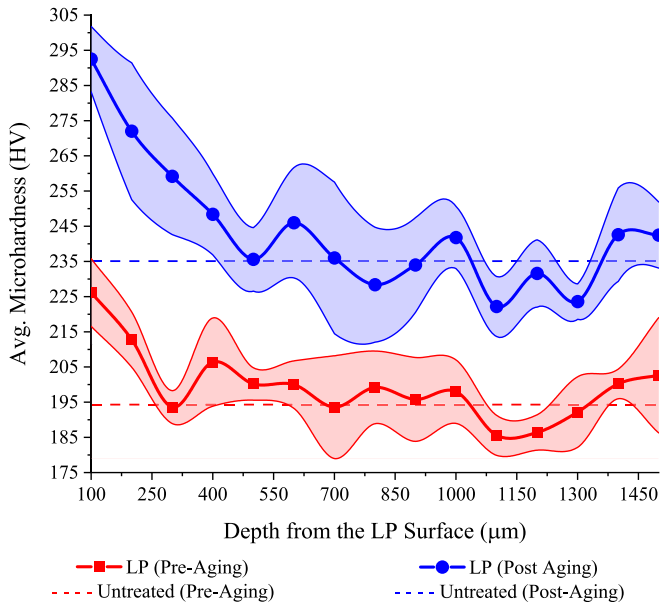

Fig. 2. Microhardness plot vs. depth for the LP pre-aging (red solid line) and post-aging (blue solid line) as well as the untreated material pre-aging (red dotted line) and post-aging (blue dotted line). The shaded regions represent the standard deviation associated with each data point, which is the average of 5 microindentation tests. (For interpretation of the references to colour in this figure legend, the reader is referred to the web version of this article.)

3.2. Grain size and orientation

Figs. 3 (a-c) show EBSD scans taken from as-cast, as-cast + HT, and LP + HT respectively. Perhaps the most immediately noticeable feature is the large degree of annealing twins present in all samples. Annealing twins form to alleviate internal energy within the atomic lattice and were likely formed during the casting process and are noted by the sharp boundary lines within the parent grains. The degree of twinning between all samples (including as-cast) appeared to remain constant throughout the various treatment schemes and therefore is not considered to be a by-product of any post-processing LP or thermal treatment. The grain size distribution plot in Fig. 3d shows that most grain diameters ranged between approximately 50 μm to 150 μm with some grains exceeding 400 μm (not shown on the graph for clarity). Moreover, the overall grain texture remains unchanged as each sample shows a random distribution of grain orientations. Again, this distribution does not change after LP, aging, or LP + aging and is therefore not regarded as a strengthening mechanism.

3.3. Carbides

The lack of change in grain morphology was expected as the heat treatment utilized in this work was directly aimed at the precipitation and growth of beneficial second-phase particles. Carbides in IN617 are generally deemed strengthening phases as they are able to pin grain boundaries [26] and inhibit dislocation movement in sufficient quantities and distributions [25–27]. However, the microstructure of IN617 in the as-cast condition is far from optimal as the carbides gather in distinct bands (Fig. 4a). These bands tend to coincide with the hot rolling direction [27] and result in a microstructure with heterogeneous mechanical properties. Additionally, a discrete dispersion of Ti(C, N) particles can be seen both within grains as well as at grain boundaries (Fig. 4c and d) [27,28]. The carbides are very small with a diameter of ~100 nm while the Ti(C, N) particles are comparatively much larger at ~25 to 50 μm (Fig. 4d) [29,30]. Interestingly, the carbides also group themselves into cellular structures, which was theorized by [27] to be a result of precipitation on grain boundaries which were present prior to hot rolling. In addition to the irregular arrangements of carbides, the lack of developed γ' precipitates allows for easier movement of dislocations upon plastic loading and consequently leads to the as-cast specimen having the lowest microhardness of any test specimen (Fig. 2). Therefore, heat treatment is typically conducted to homogenize the microstructure and bring the precipitates to peak size, shape, and distribution.

SEM images taken of the aged specimen (Fig. 4b) depict a change in precipitate distribution with carbides largely now spread across the microstructure in a much more homogenous dispersion. The carbide bands have not disappeared (the heat treatment temperature was not sufficient to cause dissolution as described by Mankins et al. [29]), but they are obscured by the precipitation of additional carbides. Interestingly, the carbides appear to have grown very little, if at all, after aging. Wang et al. [31] reasoned that the slow growth is due to the increasing dominance of Cr + Mo and Mo as the metal component of $M_{23}C_6$ and M_6C type carbides respectively as aging times progress. The slow diffusion rates of Cr and Mo at 650 °C greatly limit carbide growth during aging and are the primary factor in carbide size remaining relatively unchanged. An additional point of consideration is that the depletion of Cr and Mo from the γ matrix causes a reduction in solid solution strengthening. Thus, there are competing strengthening mechanisms that must be considered when designing a treatment process. In the case of the aging conducted in this work, the 60-h aging time is far below the time in which Wang et al. found Cr and Mo depletion from the matrix to become dominant (>650 h) and therefore is not considered as a potential weakening mechanism.

While the SEM and OM images provided key insights into the carbide and nitride precipitation behavior post heat treatment, there remain questions regarding the precipitation of new phases. Specifically, the aging treatment chosen was designed to precipitate and grow γ', Ti(C, N), M_6C, and $M_{23}C_6$ as these were the thermodynamically stable phases under the given heat treatment conditions. Fig. 5 shows the data from XRD scans taken at the surface of all samples and shows that γ', Ti(C, N), M_6C, and $M_{23}C_6$ are all present, validating that the heat treatment functioned as intended.

3.4. γ' precipitates

In addition to carbides and nitrides, the strengthening phase, γ', is known to form at 650 °C, and thus further investigation was required to determine the extent to which γ' precipitation and growth added to the overall inhibition of dislocation movement. As shown by the TTT diagram in Fig. 1d, γ' precipitates begin forming after around 1-h at 650 °C, though their volume fraction and diameter are highly underdeveloped at this stage [31,32]. Fig. 6a and b show dark field TEM images of the as-cast + HT and LP + HT and corresponding SAED pattern centered around the $< 1\overline{1}2 >$ zone axis showing the superlattice reflection of the γ' particles. Particle diameter and area fraction were then calculated using the ImageJ software package. The average diameter of γ' in both samples was 8 nm and the area fraction was ~12.5% respectively. This coarsening behavior is consistent with the Lifshitz-Slyozov-Wagner (LSW) model for the asymptotic stage of Ostwald ripening [33,34] (as was shown by [31]) where particle radius (r) and aging time (t) maintain the following relationship $r(t) \propto t^{\frac{1}{3}}$. Experimental data from [31] shows that this relationship only exists at short aging times (as was used in this work) as precipitate coarsening rates deviate significantly from the LSW model at time > 20,000 h.

It is worth mentioning that given the precipitate size and distribution are observed to be identical between the LP + HT and as-cast + HT conditions and thus it can be said that LP had little if any, effect on the precipitation kinetics under the short-term aging conditions chosen for this study. It is hypothesized that because the thermodynamic driving force for γ' precipitation is large at the onset of aging [35], the addition of otherwise energetically-favorable nucleation sites provided by

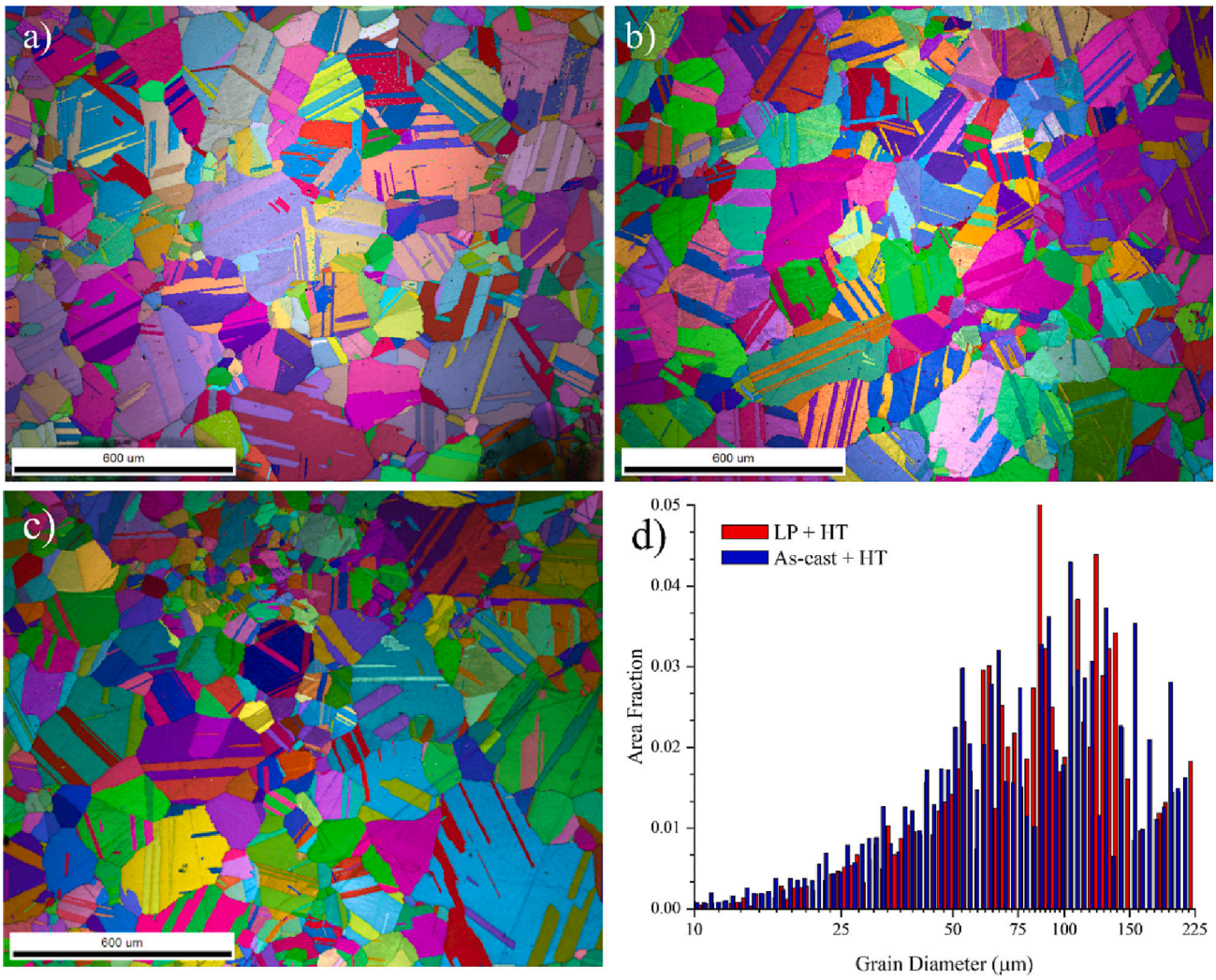

Fig. 3. EBSD IPF + IQ maps of the (a) as-cast microstructure, (b) as-cast + HT, and (c) LP + HT specimen near the treated surface. (d) The grain diameter distribution bar graph comparing the as-cast + HT and LP + HT specimens show a very similar distribution, indicating that LP has no effect on grain size or orientation under these conditions.

dislocations in the LP specimen was not favorable enough to drive heterogeneous precipitation. That is not to say that the dislocations did not play a role in precipitation dynamics here, but their contribution was likely non-dominant.

3.5. Dislocations

The localized plastic deformation caused by LP results in a strain mismatch, and consequently develops a compressive residual stress state that directly aids in resistance to surface-initiated damage mechanisms. As a result, any relaxation in plastic strain in the presence of thermal loading will directly cause a degradation in the beneficial residual stress field, rendering the surface treatment largely ineffective. When designing an LP treatment, it is important to discuss the density, distribution, and potential rearrangement of dislocations. Fig. 7a shows a STEM image taken from the as-cast material. It can be seen that the dislocation density is very low with a few dislocations (likely created during manufacturing) travelling in pairs through an otherwise defect-free microstructure. Dislocation pairs form out of necessity to restore the anti-phase boundary created by the shearing of an ordered precipitate phase [36], which in this case takes the form of γ'. Following LP, the dislocation density greatly increased with several curved dislocation lines as well as dislocation pairs (Fig. 7b). The curvature in the dislocations represents a deviation from their original glide path, which occurs due to interactions with other dislocations and/or γ' precipitates. The γ' particles are very small and thus primarily interact with dislocations through a strongly coupled shearing mechanism [36]. While the γ' precipitates are not visible in these images, their presence is again recognized by dislocation curvatures. Fig. 7c and d show representative images of carbides interacting with dislocations in the as-cast and LP + HT specimens respectively. The carbides are comparatively much larger than the γ' particles and consequently interact with dislocations very differently. Pileups and tangles are visibly present around the borders of the carbide (Fig. 7d) which is beneficial in terms of mechanical strength as these dislocations are unable to bypass or shear through the carbide and will slow additional dislocation movement upon further plastic loading [37].

3.6. Work hardening model

From the microstructural data presented thus far, it is clear that LP and aging had distinct strengthening effects on the microstructure and microhardness of IN617. However, these effects appear to be mutually exclusive and the following discussion is meant to analyze the contribution of each mechanism to the overall hardness enhancements provided by LP and aging. Beginning with the work-hardening aspect of LP,

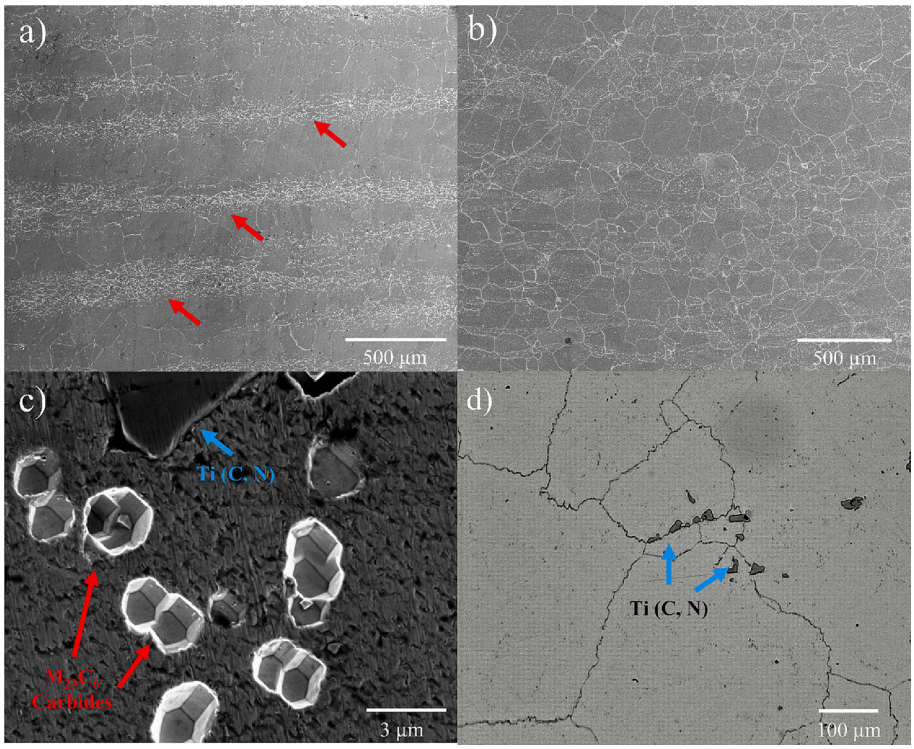

Fig. 4. SEM images of (a) the as-cast material showing distinct carbide bands marked with red arrows and (b) carbides migrating into a more homogenous dispersion after aging treatment. (c) Ti(C, N) and $M_{23}C_6$ particles are shown in detail. (d) Representative optical microscope (OM) image of Ti(C, N) particles occupying sites at grain boundaries (GBs) marked by blue arrows. (For interpretation of the references to colour in this figure legend, the reader is referred to the web version of this article.)

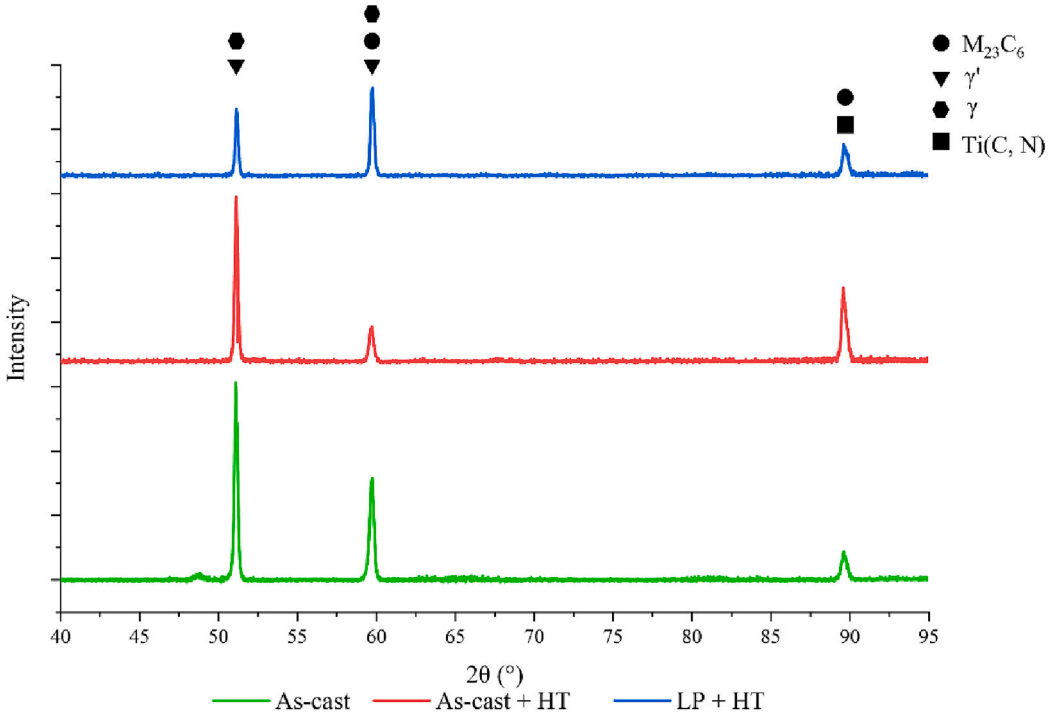

Fig. 5. XRD scans of the as-cast (black), as-cast + HT (red), and LP + HT (blue) showing peaks corresponding to metal carbides, γ', and Ti(C, N) with no additional phases precipitated during the heat treatments stage. (For interpretation of the references to colour in this figure legend, the reader is referred to the web version of this article.)

a slightly modified version of Taylor's Eq. [32] was used to calculate the contribution of dislocations to enhanced strength [38,39]:

$$\Delta H_{TH} = \alpha G b \sqrt{\rho} \quad (1)$$

where ΔH_{TH} is the change in Vickers microhardness due to work hardening, G is an isotropic shear modulus of 81 GPa [31], b is the magnitude of the Burgers vector of 0.248 nm and the geometric parameter, α, is 0.25 (typically on the order of 0.1–1). Dislocation density 'ρ' was calculated by Eq. 2 using the line intercept method [38] where N is the number of dislocations intersected by the line, L is the line length, and t is the lamella thickness (70 nm). The TEM foil was taken at

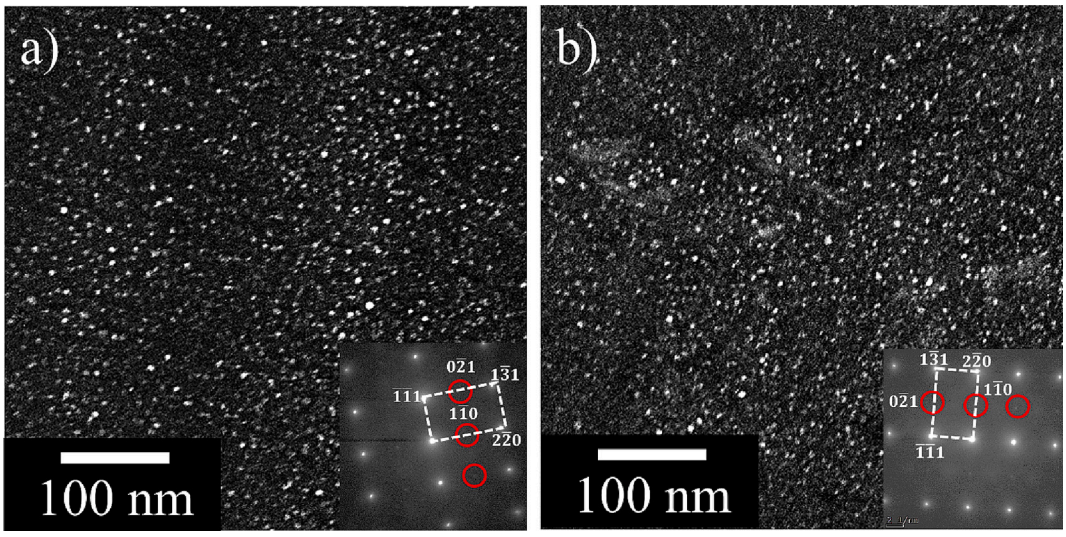

Fig. 6. Dark field TEM images and corresponding diffraction pattern showing the superlattice reflection from the γ' particles from the (a) as-cast + HT specimen and (b) LP + HT specimen. Lamellas were taken 50 μm from the LPed surface.

a depth of 50 μm to correspond with the depth of the first row of microindents.

$$\rho = \frac{2N}{Lt} \tag{2}$$

Given a dislocation density of 3×10^{14} lines/m^2, the Taylor hardening component of microhardness enhancement following laser peening is then ~70 HV, which corresponds well with the observed increase of ~60 HV. The small discrepancy between the theoretical and experimental hardness enhancement can be accounted for by the 'α' parameter which is only an approximate value. Additionally, Krishna et al. show that an error of ±20 HV is common in this calculation which could also explain the apparent lack of contribution of residual stresses to the microhardness increase. It may also be said that dislocation movement, and thus plasticity, is governed nearly entirely by dislocation-dislocation and dislocation-precipitate interactions, whereas at greater depths from the LP surface, the residual stresses may dominate.

3.7. Precipitation hardening model

The next phase of analysis involves the calculation of the precipitation hardening component. The aging treatment applied to the as-cast and LPed material was designed to induce the precipitation of carbides, nitrides, and γ'. The contributions of carbides and nitrides are significant but are relatively low in comparison to the contributions of γ' for this aging time and temperature range [31]. The Jackson-Reed model was then employed to quantify the role of γ' in the precipitation hardening behavior due to its ability to account for the shearing of the ordered γ' phase by strongly coupled dislocation pairs, which is the primary mechanism of dislocation passage through a precipitate at the small sizes seen in the aged specimens [31]. The model is as follows:

$$\Delta\sigma_{y,Jackson-Reed} = \left(\frac{MGb}{r}\right)(1.5\varphi)^{\frac{1}{2}}\left(\frac{w}{\pi^{\frac{3}{2}}}\right)\left(\frac{2\pi\gamma_{apb}\bar{r}}{wGb^2} - 1\right)^{\frac{1}{2}} \tag{3}$$

where $\Delta\sigma_{y,Jackson-Reed}$ is the change in yield strength according to the Jackson-Reed model, M is the Taylor factor, r is precipitate radius, w is a parameter related to the elastic repulsion between strongly coupled dislocation pairs [40] (0.42 in this case [31]), and γ_{apb} is the anti-phase boundary energy (0.1 for this alloy [41,42]).

The volume fraction term, φ, is not equivalent to the area fraction term calculated by image analysis from the dark field TEM images. This is because TEM images are two-dimensional projections of a three-dimensional lamella and the average diameters of γ' precipitates are very small relative to the lamella thickness. Consequently, acknowledgment must be given to the overlap of precipitates which lie at different depths throughout the lamella to obtain a precise volume fraction. Krishna et al. [32] determined that this can be achieved via the following relationship from the Kolmogorov–Johnson–Avrami–Mehl equation:

$$\varphi = 1 - \left(1 - A_f\right)^m \tag{4}$$

$$m = \frac{4.32r}{3t + 4.32r} \tag{5}$$

where φ is volume fraction, A_f is area fraction, and m is an exponent described by particle radius, r, and lamella thickness, t. As discussed in Section 2.3, A_f is 12.5%, r is 4 nm, and t is 70 nm. Plugging in these values yields a volume fraction (φ) of 1.2% which is consistent with [43], where a similar time and temperature were used.

Following the determination of the volume fraction, one can proceed with the Jackson-Reed calculation. Of course, this equation solves for the increment of yield strength added by the precipitation of γ' phases and therefore necessitates a conversion to hardness for this discussion. This can be achieved by the following relation:

$$\Delta H_{Jackson-Reed} = \frac{1}{\beta}\sigma_{y,Jackson-Reed} \tag{6}$$

where $\Delta H_{Jackson-Reed}$ change in hardness after γ' precipitation according to the Jackson-Reed model and β is a coefficient, and $\sigma_{y,Jackson-Reed}$ is measured in MPa. Osada et al. [44] determined that the value of β for precipitation-strengthened Ni-based superalloys such as IN617 is 2.46, which yields a hardness increase of 43.6 HV due to γ' precipitation during the aging process. This compares very favorably to the 40 HV increase measured via microindentation. From the experimental and model data, it can be inferred that the precipitation of γ' particles is the primary mechanism behind the increased hardness following aging with the precipitation and potential growth of carbides and nitrides playing a minor role. Wang et al. found that carbides and nitrides are only expected to contribute <10 HV after much longer aging times (>5000 h) [31].

When looking at the data overall, the key takeaway is that the LP and aging treatments greatly strengthen the surface and would certainly allow the material to perform more favorably in conditions where resistance to surface-initiated damage mechanisms is important.

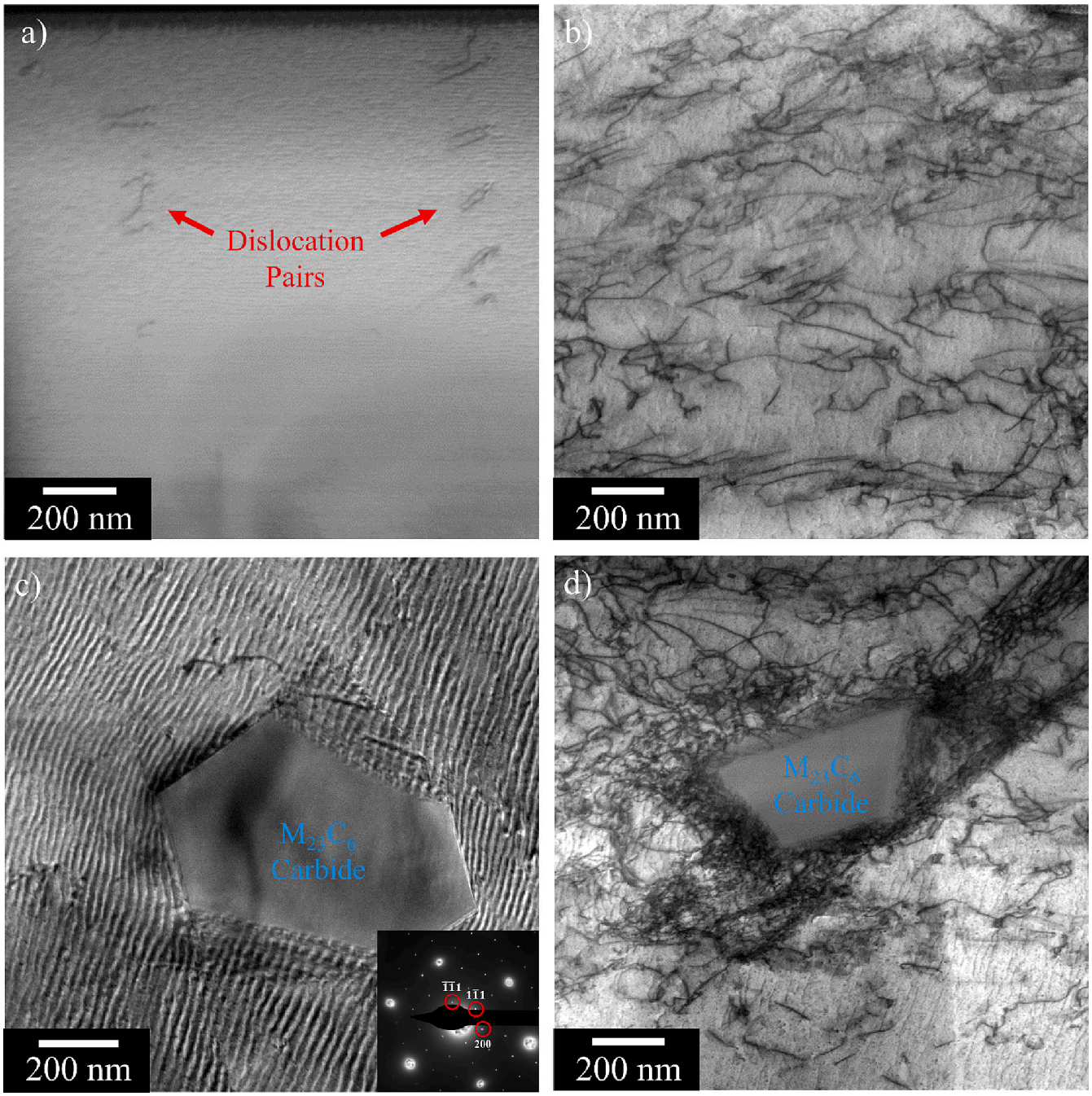

Fig. 7. (a) STEM image of the as-cast material showing low defect density. (b) A STEM image taken near the treated surface of the LP + HT specimen showing a vast increase in dislocation density. Carbides embedded within the microstructure are seen (c) prior to and (d) following LP. The dislocations created by LP tangle and pileup at the carbide phase boundary.

Additionally, the heat treatment did not degrade any beneficial effects imparted by LP, but rather only acted to further enhance the surface hardness due to the superposition of strengthening mechanisms. Unlike other combined thermal and LP techniques, the authors do not observe clear evidence of nucleation sites occurring at defects, but this is only preliminary data. It stands to reason that at much longer aging times when the driving force for precipitation continues to decrease as the microstructure moves toward an energetically favorable condition, the dislocations could provide much more favorable nucleation sites.

4. Conclusion

Inconel 617 shows immense promise as a material for VHTR components which demand high tolerance to thermal and mechanical loading. This work aimed to further magnify the structural fidelity of IN617 through the use of laser peening and aging treatment. The LPed material showed enhanced resistance to localized plastic deformation with a ~ 16% increase in microhardness over the baseline material. Interestingly, although the baseline material showed a substantial increase in microhardness after 60-h aging heat treatment at 650 °C, the microhardness near the LP-treated surface did not regress to the baseline value and rather further elevated to a value of 292 HV. Microhardness data indicated that the strengthening from the LP + aging treatments was from mutually exclusive mechanisms. This was confirmed through TEM data which showed that precipitate size and distribution showed no significant difference between the LP + HT and as-cast + HT specimens.

Additionally, SEM images showed that the carbide banding present in the as-cast specimen was dispersed into a more homogenous distribution after aging, which may have aided in the microhardness elevation. Finally, the Jackson-Reed and Taylor models were applied to the data and were found to accurately predict, giving more credence to the notion that the mechanisms were independent of one another. The combined effects of work hardening from LP and precipitation hardening from aging led to a stronger microstructure which is highly beneficial to industrial applications which require high resistance to wear and surface-initiated damage mechanisms. With the data collected in this work, the authors hope to progress the scientific knowledge on a very capable material for next-generation nuclear reactors, and therefore aid in the progression toward a more sustainable future.

Funding

The project was supported by the National Science Foundation, CMMI, and Advanced Manufacturing Program (Award Number: 2029059).

Declaration of Competing Interest

The authors declare that they have no known competing financial interests or personal relationships that could have appeared to influence the work reported in this paper.

Data availability

Data will be made available on request.

Acknowledgment

The authors would like to thank Idaho National Lab (INL) for providing raw Inconel 617 specimens as well as Dr. Andreas A. Polycarpou and Dr. Ali Beheshti.

References

[1] Technology roadmap update for generation IV nuclear energy systems, in: Gen IV International Forum, OECD Nuclear Energy Agency, 2014.
[2] R. Baranwal, 10 Big Wins for Nuclear Energy in 2020, Available from: energy.gov, 2020.
[3] P.S. Shankar, K. Natesan, Effect of trace impurities in helium on the creep behavior of alloy 617 for very high temperature reactor applications, J. Nucl. Mater. 366 (1–2) (2007) 28–36.
[4] K. Natesan, A. Purohit, S.W. Tam, Materials Behavior in HTGR Environments, Argonne National Laboratory, 2003, p. 85.
[5] J. Hosier, D. Tillack, INCONEL alloy 617: a new high-temperature alloy, Metals Eng. Quart 12 (3) (1972) 51–55.
[6] M.S. Rahman, et al., Characterization of high temperature deformation behavior of INCONEL 617, Mech. Mater. 41 (3) (2009) 261–270.
[7] A. Ahmadi, F. Sadeghi, S. Shaffer, In-situ friction and fretting wear measurements of Inconel 617 at elevated temperatures, Wear 410-411 (2018) 110–118.
[8] M.S. Rahman, et al., Elevated temperature tribology of Ni alloys under helium environment for nuclear reactor applications, Tribol. Int. 123 (2018) 372–384.
[9] S. Salari, et al., Elevated temperature mechanical properties of Inconel 617 surface oxide using nanoindentation, Mater. Sci. Eng. A 788 (2020), 139539.
[10] V. Pauly, et al., Wear performance of incoloy 800HT and inconel 617 in various surface conditions for high-temperature gas-cooled reactor components, Tribol. Int. 154 (2021), 106715.
[11] A.A. Polycarou, High Temperature Tribology Performance of Ni alloys under Helium Environment for Very High Temperature Gas Cooled Reactors (VHTRs), 2019. United States.
[12] J.T. Wang, et al., Improving creep properties of 7075 aluminum alloy by laser shock peening, Surf. Coat. Technol. 349 (2018) 725–735.
[13] O. Hatamleh, J. Lyons, R. Forman, Laser and shot peening effects on fatigue crack growth in friction stir welded 7075-T7351 aluminum alloy joints, Int. J. Fatigue 29 (3) (2007) 421–434.
[14] S. Zabeen, M. Preuss, P.J. Withers, Evolution of a laser shock peened residual stress field locally with foreign object damage and subsequent fatigue crack growth, Acta Mater. 83 (2015) 216–226.
[15] B. Lin, et al., Fatigue crack growth in laser-shock-peened Ti–6Al–4V aerofoil specimens due to foreign object damage, Int. J. Fatigue 59 (2014) 23–33.
[16] J.Z. Lu, et al., Effects of laser peening on stress corrosion cracking (SCC) of ANSI 304 austenitic stainless steel, Corros. Sci. 60 (2012) 145–152.
[17] O. Hatamleh, P.M. Singh, H. Garmestani, Stress corrosion cracking behavior of peened friction stir welded 2195 aluminum alloy joints, J. Mater. Eng. Perform. 18 (4) (2009) 406–413.
[18] U. Sánchez-Santana, et al., Wear and friction of 6061-T6 aluminum alloy treated by laser shock processing, Wear 260 (7) (2006) 847–854.
[19] Z.P. Tong, et al., Effect of laser shock peening on wear behaviors of TC11 alloy at elevated temperature, Opt. Laser Technol. 109 (2019) 139–148.
[20] M. Munther, et al., Thermal stabilization of additively manufactured superalloys through defect engineering and precipitate interactions, Mater. Sci. Eng. A 798 (2020).
[21] M. Munther, et al., An investigation into the mechanistic origin of thermal stability in thermal-microstructural-engineered additively manufactured Inconel 718, Vacuum 199 (2022), 110971.
[22] Z. Tang, et al., The effect of warm laser shock peening on the thermal stability of compressive residual stress and the hot corrosion resistance of Ni-based single-crystal superalloy, Opt. Laser Technol. 146 (2022), 107556.
[23] Z. Tang, et al., Effect of warm laser shock peening on the low-cycle fatigue behavior of DD6 nickel-based single-crystal Superalloy, J. Mater. Eng. Perform. 30 (4) (2021) 2930–2939.
[24] Z. Tang, et al., An investigation of the effect of warm laser shock peening on the surface modifications of [001]-oriented DD6 superalloy, Int. J. Adv. Manuf. Technol. 113 (7–8) (2021) 1973–1988.
[25] Q. Wu, et al., Microstructure of long-term aged IN617 Ni-Base Superalloy, Metall. Mater. Trans. A 39 (11) (2008) 2569–2585.
[26] S.S. Katnagallu, et al., Role of carbide precipitates and process parameters on achieving grain boundary engineered microstructure in a Ni-based Superalloy, Metall. Mater. Trans. A 46 (10) (2015) 4740–4754.
[27] J. Benz, T. Lillo, R. Wright, Aging of Alloy 617 at 650 and 750 Degrees C, Idaho National Lab.(INL), Idaho Falls, ID (United States), 2013.
[28] T.S. Jo, et al., Effects of grain refinement on internal oxidation of alloy 617, J. Nucl. Mater. 402 (2) (2010) 162–166.
[29] W. Mankins, J. Hosier, T. Bassford, Microstructure and phase stability of Inconel alloy 617, Metall. Mater. Trans. B Process Metall. Mater. Process. Sci. 5 (12) (1974) 2579–2590.
[30] W.L. Mankins, J.C. Hosier, T.H. Bassford, Microstructure and phase stability of INCONEL alloy 617, Metall. Mater. Trans. B Process Metall. Mater. Process. Sci. 5 (12) (1974) 2579–2590.
[31] Z. Wang, et al., On the kinetics of gamma prime (γ') precipitation and its strengthening mechanism in alloy 617 during a long-term thermal aging, Materialia 11 (2020), 100682.
[32] R. Krishna, et al., Gamma prime precipitation, dislocation densities, and TiN in creep-exposed Inconel 617 alloy, Metall. Mater. Trans. A 47 (1) (2016) 178–193.
[33] I.M. Lifshitz, V.V. Slyozov, The kinetics of precipitation from supersaturated solid solutions, J. Phys. Chem. Solids 19 (1) (1961) 35–50.
[34] C. Wagner, Theorie der Alterung von Niederschlägen durch Umlösen (Ostwald-Reifung), Z. Elektrochem. Ber. Bunsenges. Phys. Chem. 65 (7–8) (1961) 581–591.
[35] K.B.S. Rao, et al., Influence of time and temperature dependent processes on strain controlled low cycle fatigue behavior of alloy 617, Metall. Trans. A. 19 (2) (1988) 359–371.
[36] A. Goodfellow, Strengthening mechanisms in polycrystalline nickel-based superalloys, Mater. Sci. Technol. 34 (15) (2018) 1793–1808.
[37] S. Chomette, J.M. Gentzbittel, B. Viguier, Creep behaviour of as received, aged and cold worked INCONEL 617 at 850°C and 950°C, J. Nucl. Mater. 399 (2) (2010) 266–274.
[38] H. Zhang, et al., Microstructure and mechanical properties of laser shock peened 38CrSi steel, Mater. Sci. Eng. A 788 (2020), 139486.
[39] L. Tian, A. Russell, I. Anderson, A dislocation-based, strain–gradient–plasticity strengthening model for deformation processed metal–metal composites, J. Mater. Sci. 49 (7) (2014) 2787–2794.
[40] W. Hüther, B. Reppich, Order hardening of MgO by large precipitated volume fractions of spinel particles, Mater. Sci. Eng. 39 (2) (1979) 247–259.
[41] R.C. Reed, The Superalloys: Fundamentals and Applications, Cambridge University Press, 2008.
[42] B. Reppich, Some new aspects concerning particle hardening mechanisms in γ'precipitating Ni-base alloys—I. Theoretical concept, Acta Metall. 30 (1) (1982) 87–94.
[43] H.-J. Penaklla, J.W, E.V. Fisher, F. Schubert, Proc. 5th International Symposium on Superalloys 718, 625, 706, and Derivatives, 2001. Pittburgh, Pennsylvania.
[44] T. Osada, et al., Optimum microstructure combination for maximizing tensile strength in a polycrystalline superalloy with a two-phase structure, Acta Mater. 61 (5) (2013) 1820–1829.